

## Article

# Mandarin Peels-Derived Carbon Dots: A Multifaceted Fluorescent Probe for Cu(II) Detection in Tap and Drinking Water Samples

Marwa El-Azazy <sup>1,\*</sup>, Alaa AlReyashi <sup>1</sup>, Khalid Al-Saad <sup>1</sup>, Nessreen Al-Hashimi <sup>1</sup>,  
Mohammad A. Al-Ghouti <sup>2</sup>, Mohamed F. Shibl <sup>3</sup>, Abdulrahman Alahzm <sup>1</sup> and Ahmed S. El-Shafie <sup>1,\*</sup>

<sup>1</sup> Department of Chemistry and Earth Sciences, College of Arts and Sciences, Qatar University, Doha 2713, Qatar; aa1906650@student.qu.edu.qa (A.A.)

<sup>2</sup> Environmental Sciences Program, Department of Biological and Environmental Sciences, College of Arts and Sciences, Qatar University, Doha 2713, Qatar; mohammad.alghouti@qu.edu.qa

<sup>3</sup> Chemistry Department, Faculty of Science, Cairo University, Giza 12613, Egypt

\* Correspondence: marwasaid@qu.edu.qa (M.E.-A.); aelshafie@qu.edu.qa (A.S.E.-S.); Tel.: +974-4403-4675 (M.E.-A.); Fax: +974-4403-4651 (M.E.-A. & A.S.E.-S.)

**Abstract:** Carbon dots (CDs) derived from mandarin peel biochar (MBC) at different pyrolysis temperatures (200, 400, 600, and 800 °C) have been synthesized and characterized. This high-value transformation of waste materials into fluorescent nanoprobe for environmental monitoring represents a step forward towards a circular economy. In this itinerary, CDs produced via one-pot hydrothermal synthesis were utilized for the detection of copper (II) ions. The study looked at the spectroscopic features of biochar-derived CDs. The selectivity of CDs obtained from biochar following carbonization at 400 °C (MBC400-CDs towards various heavy metal ions resulted in considerable fluorescence quenching with copper (II) ions, showcasing their potential as selective detectors. Transmission electron microscopic (TEM) analysis validated the MBC-CDs' consistent spherical shape, with a particle size of <3 nm. The Plackett–Burman Design (PBD) was used to study three elements that influence the  $F_0/F$  ratio, with the best ratio obtained with a pH of 10, for 10 min, and an aqueous reaction medium. Cu (II) was detected over a dynamic range of 4.9–197.5  $\mu\text{M}$  and limit of detection (LOD) of 0.01  $\mu\text{M}$ . Validation testing proved the accuracy and precision for evaluating tap and mountain waters with great selectivity and no interference from coexisting metal ions.

**Keywords:** carbon dots; mandarin peels biochar; hydrothermal process; Plackett–Burman Design; fluorescence sensor; copper (II) detection



**Citation:** El-Azazy, M.; AlReyashi, A.; Al-Saad, K.; Al-Hashimi, N.; Al-Ghouti, M.A.; Shibl, M.F.; Alahzm, A.; El-Shafie, A.S. Mandarin Peels-Derived Carbon Dots: A Multifaceted Fluorescent Probe for Cu(II) Detection in Tap and Drinking Water Samples. *Nanomaterials* **2024**, *14*, 1666. <https://doi.org/10.3390/nano14201666>

Academic Editors: Marcel Popa and Leonard Ionut Atanase

Received: 16 September 2024

Revised: 9 October 2024

Accepted: 15 October 2024

Published: 17 October 2024



**Copyright:** © 2024 by the authors. Licensee MDPI, Basel, Switzerland. This article is an open access article distributed under the terms and conditions of the Creative Commons Attribution (CC BY) license (<https://creativecommons.org/licenses/by/4.0/>).

## 1. Introduction

Carbon dots (CDs) are carbon-based materials of the nanoscale size range that have garnered attention in many scientific and technological fields. Thanks to their unique attributes, CDs hold potential for diverse applications: in electronics, as sensors, for bioimaging, drug delivery, and catalysis. Their unique quality is evident in their optical attributes, with significant photoluminescence yield, great sensitivity, and capability to operate in a concentration-dependent manner [1–5]. Therefore, CDs are often employed as sensing materials for numerous environmental pollutants, including, but not limited to, heavy metals [5–8]. Compared to the traditional molecular sensors, CDs are photostable, biocompatible and are readily surface-functionalized, which increases their solubility and allows for specific interactions with the target pollutant [9,10].

Recently, biomasses have gained a growing significance as carbon precursors for CDs due to their abundance and the existence of heteroatoms, facilitating self-doping and resulting in excellent properties of the synthesized CDs [11–14]. One of the key benefits of using

biomasses for environmental applications is their abundance and lower toxicity, as compared to the synthetic carbon sources. Consequently, turning biomasses into CDs can boost the development and uses of CDs while lowering concerns of environmental pollution.

Additionally, biomasses can be converted into biochar via thermal treatment in an oxygen-deficient environment. The use of biochar as an adsorbent for a variety of environmental remediation applications has been widely reported and could be comprehended based on its unique attributes such as large surface area, carbon-rich structure, porosity, etc. [15–17]. On the other hand, applications entailing the use of biochar as carbon precursor for CDs are not as anticipated [18–20]. Several benefits could be garnered by using biochar as a precursor. To start with, and since biochar is made from biomass waste, it represents a sustainable approach that helps reduce total ecological impact via carbon fixation [21]. Furthermore, the synthesis of CDs on a large scale can be made economically feasible by using biochar, which is inexpensive and frequently derived from easily accessible resources [22]. The prevalence of functionalities like hydroxyl and carboxyl groups on the biochar surface facilitates the stabilization and surface functionalization of CDs [23]. On the other hand, synthesis of CDs using other carbon precursors might encounter some drawbacks, as illustrated in Table 1.

**Table 1.** The disadvantages of some precursors used for the synthesis of CDs.

Precursor	Drawbacks
Citric acid	One drawback is the complicated and poorly understood chemical mechanism that produces CDs from citric acid [24]. It can be challenging to regulate the optical characteristics of CDs made from citric acid, resulting in changes in their fluorescence and quantum yields [25]. Citric acid-synthesized CDs might also lack long-term photostability, which is crucial for bioimaging applications [26].
Glucose	Strong absorption in the observable range of wavelengths is a characteristic of glucose-based CDs that may restrict their use in some fields [27]. Also, producing CDs from glucose may involve complicated and time-consuming processes and toxic chemicals, leading to higher production costs [28].
Graphene	The high cost of synthesis and the possibility of contamination by strong acids are the major drawbacks of employing graphene as a carbon precursor [29,30].

In this vein, several methods have been reported in the literature for the synthesis of CDs from their carbon precursors [5]. Yet, the hydro/solvothermal approach remains as one of the most reported routes, offering notable benefits in terms of cost-effectiveness, greenness, controllability, and simplicity [31,32].

Copper is recognized as a necessary micronutrient and a vital component for the survival of all living organisms, as it plays a crucial role in a variety of physiological processes [33–35]. Humans possess intrinsic mechanisms for regulating optimal copper levels within their bodies; however, surpassing the required limit can result in toxic symptoms such as vomiting, diarrhea, stomach aches, nausea, and a metallic taste. Also, excessive ingestion of copper ions, possibly from contaminated water sources, can cause a variety of health problems, affecting the liver or kidneys and causing gastrointestinal disorders [36]. The recommended daily copper consumption for healthy individuals is 900 µg/day, while newborns should consume up to 340 µg/day. Levels of copper present in the human body range from 1.4 to 2.1 mg/kg of body mass and are essential for sustaining a balanced metabolism. The US Environmental Protection Agency (EPA) has set a maximum limit copper level of 1.3 milligrams per liter [33].

By and large, several well-established analytical techniques have been reported in the literature for the determination of copper in different matrices with high sensitivity and selectivity. Commonly reported methods include the elemental analysis techniques such as inductively coupled plasma optical emission spectroscopy (ICP-OES), its mass spectrometry counterpart (ICP-MS), and atomic mass spectroscopy (AAS) [36,37]. ICP-MS, ICP-OES, and AAS are well-established analytical tools for copper analysis. ICP-MS is versatile, with

low detection limits and multi-elemental analysis capabilities, but it requires sophisticated instrumentation and expert operators, making it costly to set up and operate [38]. While AAS is simpler and less expensive, it may lack sensitivity and multi-element capabilities, restricting its use to complicated matrices or trace-level analysis [39]. Sample preparation for these techniques can be time-consuming and involve the use of solvents and corrosive acids, raising safety concerns, while interference from matrix components can impair accuracy, demanding careful calibration [40]. Calibration standards and quality control methods are required for all techniques, which increases the overall analysis cost and time [41].

In the current approach, CDs derived from waste mandarin biochar has been employed as a sensitive and selective sensor for copper ions. Controlling the sensing process parameters while targeting the maximum fluorescence intensity (FI), and hence sensitivity, has been approached using Plackett–Burman design (PBD), offering multiple benefits, including less consumption of chemicals, less generation of waste, and implying a greener process [42,43]. The novelty of this work, therefore, stems from the facile, cost-effective, and ecofriendly synthesis of CDs from a natural and abundantly available waste, mandarin peels. This high-value transformation of waste materials into fluorescent nanoprobe for environmental monitoring represents a step forward towards a circular economy. Recycling of the waste materials into CDs offers a sustainable solution to waste disposal while creating a valuable, carbon-based nanosensor. The current approach not only reduces the negative impact of waste disposal, but it also provides a new pathway to produce CDs, with potential applications in the sensing of heavy metals. Additionally, it diminishes the demand for non-renewable resources.

A comprehensive spectroscopic characterization of the synthesized CDs has been approached. Furthermore, the selectivity of the prepared CDs towards copper (II) ions has been confirmed and compared to an array of other metal ions. The performance of the developed nanoprobe has been optimized, operating a parametric design control. Having developed these novel nano-probes, we have extended their application to real-world scenarios by testing their capability to detect the presence of copper in tap and mountain drinking waters. With a limit of detection as low as 0.01  $\mu\text{M}$ , the high sensitivity is guaranteed in real samples where the copper (II) concentration is  $\sim 20 \mu\text{M}$ , as outlined by the US EPA. Comprehensive method validation has been fully depicted following the ICH guidelines.

## 2. Materials and Methods

### 2.1. Materials and Chemicals

Mandarin peels, which were bought from a local grocery store, were utilized to prepare the biochar (MBC). All the samples were dissolved in deionized water (DIW) acquired from the Millipore-Q system (Burlington, MA, USA). All chemicals were procured from Sigma-Aldrich (St. Louis, MO, USA). Quinine sulfate was utilized as a standard reference material to measure quantum yield (%QY). Iron (III) chloride anhydrous, tin (II) chloride, lead (II) acetate basic, cadmium (II) nitrate, chromium (III) chloride-6-hydrate, nickel (II) acetate tetrahydrate, and copper (II) acetate monohydrate were all used for the selectivity testing. Acetonitrile (ACN) and DIW were used as reaction media for the experimental design. Tap water was collected from laboratory facilities at Qatar University, and drinking water, which is imported from Lebanon with no label for the copper content on the bottle, was purchased from a Qatari supermarket.

### 2.2. Instruments

A Teflon-lined stainless-steel autoclave was used to carry out the reaction under high temperature. An ultra-sonicator (SONYCLEAN PTY. Ltd., Adelaide, Australia) was utilized for proper mixing. The samples were filtered using regular filter paper and refiltered using a 0.45  $\mu\text{m}$  syringe filter. A UV lamp (SPECTROLINE<sup>®</sup>, Model CM-10A, Melville, NY, USA) was used to observe the fluorescence. The excitation wavelength was determined using

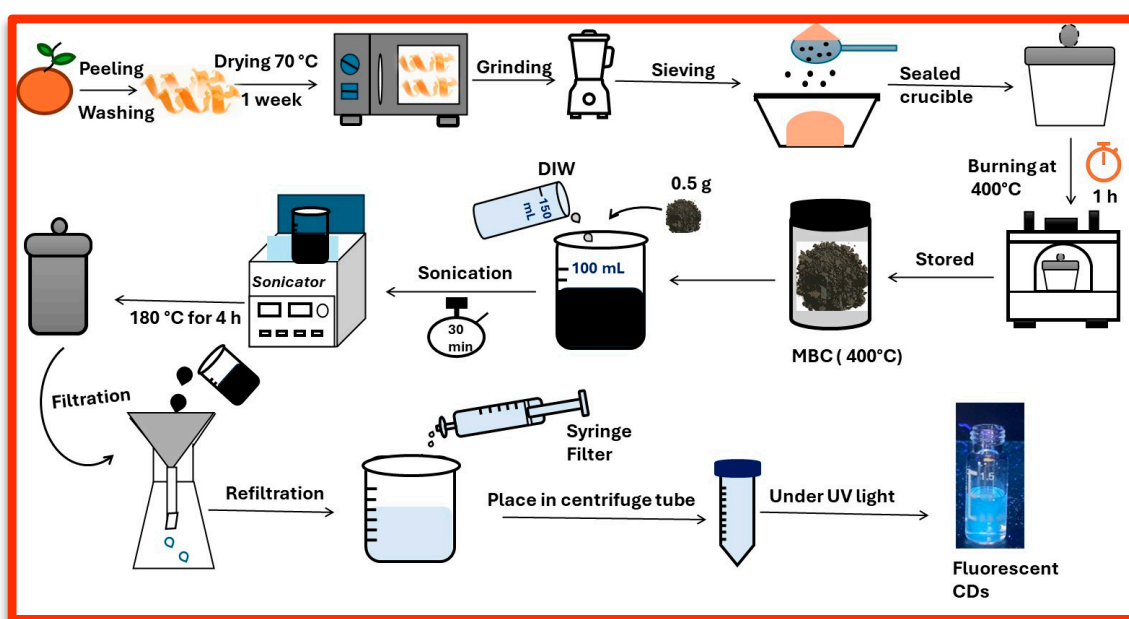
a UV–vis spectrophotometer (Agilent diode-array, Agilent, Santa Clara, CA, USA) with matched quartz cuvette cells. A Shimadzu (RF-6000, Kyoto, Japan) spectrofluorometer fitted with a  $1 \times 1$  cm quartz fluorescent cuvette was used to perform fluorescence intensity (FI) measurements. The surface function groups of the produced CDs were analyzed using FT-IR spectroscopy (Perkin Elmer, Shelton, CT, USA). The morphology of the CDs was investigated using a Transmission electron microscope (TEM) (FEI Tecnai G2 S Twin FEG, Hillsboro, OR, USA) and Zen2.6 Lite software was used for calculating the particle size distribution. An X-ray diffractometer (X'Pert-Pro MPD, PANalytical Co., Almelo, The Netherlands) was used to perform the X-ray diffraction (XRD) investigation and a  $2\theta$  range of  $5\text{--}90^\circ$  was used for the measurements.

### 2.3. Preparation of Mandarin Peel Biochar (MBC)

The process involved removing the peels from mandarin fruit and rinsing them with tap water, followed by several washes with DIW. Subsequently, the peels were subjected to a temperature of  $70^\circ\text{C}$  in an electric oven (Memmert, GmbH + Co. KG, Schwabach, Germany) for a duration of one week. The dried peels were turned into powder using a high-speed multi-function comminutor and then sieved through a  $0.125$  mm sieve to get rid of any large particles. The mandarin powder obtained was divided into four equal portions, where each portion was burnt at a specific temperature. Therefore, the 4 samples were placed into ceramic crucibles, compressed to eliminate any air bubbles, covered tightly, and heated in a furnace at different temperatures:  $200^\circ\text{C}$ ,  $400^\circ\text{C}$ ,  $600^\circ\text{C}$ , and  $800^\circ\text{C}$ , respectively, for 60 min. The resulting material was marked as (MBC) and was stored in centrifuge tubes.

### 2.4. Synthesis of the CDs

Mandarin peel biochar MBC ( $0.5000 \pm 0.0001$  g) was dispersed in 150 mL of DIW. Then, sonication was carried out for a duration of 30 min. The solution was transferred into a Teflon-lined autoclave and placed inside the oven at  $180^\circ\text{C}$  for 4 h. The autoclave was taken out and left to cool to room temperature. After cooling, the solution underwent filtration utilizing filter paper and re-filtered by  $0.45\ \mu\text{m}$  syringe filter. Finally, the solution was subjected to UV light to detect fluorescence. For FTIR and XRD analyses, materials were freeze-dried under vacuum for 48 h. An illustration of the synthesis procedure is revealed in Scheme 1.



**Scheme 1.** Synthesis of MBC400-CDs from waste mandarin peels.

### 2.5. Quantum Yield (QY) Measurements

Preliminary investigations included comparing the quantum yield (QY) of the CDs synthesized from the three biochars. Equation (1) was used to determine the QY, which was measured using  $1.25 \times 10^{-3}$  M of quinine sulfate dissolved in 0.1 M  $\text{H}_2\text{SO}_4$ .

$$QY = Q_r \times \left(\frac{I}{I_r}\right) \times \left(\frac{A_r}{A}\right) \times \left(\frac{\eta^2}{\eta_r^2}\right) \quad (1)$$

In this equation, Q signifies the QY of the reference material, while  $I$  and  $I_r$  stand for the integrated emission intensity areas of the CDs made for this investigation and the standard quinine sulphate, respectively. The UV absorbance of the CDs and the standard reference are denoted by the letters  $A$  and  $A_r$ . Moreover,  $\eta$  and  $\eta_r$  signify the standard reference and the CDs' refraction index, correspondingly, where  $\eta = \eta_r = 1.33$ .

### 2.6. Selectivity Testing

Solutions of CDs were scanned at various excitation wavelengths ( $\lambda_{\text{ex}}$ ), and the emission wavelength ( $\lambda_{\text{em}}$ ) was detected between 320 and 500 nm. The greatest FI was achieved at  $\lambda_{\text{ex}} = 310$  nm and  $\lambda_{\text{em}} = 410$  nm. The synthesized CDs were tested for their selectivity towards various metal ions, including iron (III), tin (II), lead (II), cadmium, chromium (III), nickel (II), and copper (II). For this purpose, stock (50-ppm) solutions of each tested material were prepared in DIW. Typically, 500.0  $\mu\text{L}$  of the CD solution (MBC400-CDs) was added into the fluorescence cuvette, followed by 500.0  $\mu\text{L}$  of buffer solution with a pH of  $(9.00 \pm 0.02)$ . 2.0 mL of DIW was then added, followed by 500.0  $\mu\text{L}$  of the analyte stock solution as well. Solution was thoroughly mixed, and the FI was measured. The ability of the tested materials to reduce FI was used to evaluate the selectivity of the synthesized CDs. The fluorescence quenching was determined by the ratio  $F_0/F$ , where  $F_0$  represents the FI of the CDs, and  $F$  represents FI at 410 nm in the presence of the tested materials. All readings were compared against a blank sample containing all reaction components except the analyte.

### 2.7. Plackett–Burman Design (PBD) Copper (II) Detection

PBD was employed to find the optimum conditions for copper (II) detection, with the aim of achieving maximum sensitivity (highest fluorescence quenching,  $F_0/F$ ). The design was generated using Minitab 20 software (State College, PA, USA). PBD is characterized by a first-order polynomial mathematical model, depicted in Equation (2) [42–45].

$$Y = \beta_0 + \sum \beta_i x_i \quad (2)$$

In this equation,  $Y$  represents the response variable,  $F_0/F$ , while  $\beta_0$  denotes the mean intercept,  $x_i$  stands for the independent variable influencing the response, and  $\beta_i$  represents the associated coefficient. Three factors were examined: contact time (CT), pH, and reaction medium (RM). Table 2 outlines these factors, along with their respective levels. The experimental design comprised 36 base runs conducted with 1 replicate each, totaling 36 runs, distributed across 1 block. Additionally, 12 central points were included in the design scenario. A stock solution of 50 ppm copper (II) was prepared in DIW, and to illustrate the experimental setting, 500.0  $\mu\text{L}$  of CDs was added to a 3.5 mL cuvette, followed by 500.0  $\mu\text{L}$  of buffer solution (with pH determined according to Table 3), 2.0 mL of the reaction medium (either DIW or ACN), and 500.0  $\mu\text{L}$  of the copper (II) stock solution. The reaction mixture was allowed to incubate for a duration ranging from 30 s to 10 min, as outlined in Table 3. All the measurements were conducted in triplicate, and in all cases, measurements were compared against reagent blanks prepared in a similar manner but excluding copper (II).

**Table 2.** Factors and their corresponding levels provided to the PBD.

Code	Numerical Variables	−1	0	+1
A	Contact time, CT (min)	0.5	5.25	10
B	pH, (pH unit)	4	7	10
Code	Categorical Variables	−1		+1
C	Reaction medium, RM	DIW		ACN
Code	Dependent Variables			
Y	Fluorescence quenching, $F_0/F$	Maximum		

**Table 3.** The PBD experimental matrix and the predicted fits (BPFITS).

Run Order	Pt Type	pH	Time	RM	$F_0/F$	BPFITS
1	1	4	10	ACN	1.2600	1.2338
2	1	4	0.5	ACN	1.2300	1.2078
3	1	10	0.5	DIW	1.7180	1.7173
4	0	7	5.25	ACN	1.3131	1.3075
5	1	10	0.50	ACN	1.5378	1.5888
6	1	4	0.50	ACN	1.2260	1.2078
7	1	10	10	DIW	1.7470	1.7703
8	1	10	0.5	ACN	1.6116	1.5888
9	1	10	10	ACN	1.5906	1.6341
10	1	10	0.5	DIW	1.7180	1.7173
11	1	4	10	DIW	1.3620	1.3099
12	1	4	0.5	DIW	1.2670	1.2806
13	0	7	5.25	DIW	1.4070	1.3933
14	1	4	0.5	ACN	1.2450	1.2078
15	1	4	10	ACN	1.2530	1.2338
16	0	7	5.25	ACN	1.3668	1.3075
17	0	7	5.25	DIW	1.3889	1.3933
18	1	10	10	ACN	1.6460	1.6341
19	0	7	5.25	DIW	1.4137	1.3933
20	0	7	5.25	DIW	1.3979	1.3933
21	1	10	0.5	ACN	1.5384	1.5888
22	0	7	5.25	DIW	1.4171	1.3933
23	1	4	10	DIW	1.2601	1.3099
24	1	10	0.5	DIW	1.7987	1.7173
25	1	4	0.5	DIW	1.2617	1.2806
26	1	4	10	DIW	1.2486	1.3099
27	1	4	10	ACN	1.2390	1.2338
28	1	4	0.5	DIW	1.2391	1.2806
29	0	7	5.25	ACN	1.2948	1.3075
30	1	10	10	DIW	1.8120	1.7703
31	1	10	10	DIW	1.8232	1.7703
32	0	7	5.25	ACN	1.2437	1.3075
33	0	7	5.25	ACN	1.3370	1.3075
34	0	7	5.25	DIW	1.4058	1.3933
35	0	7	5.25	ACN	1.2384	1.3075
36	1	10	10	ACN	1.6240	1.6341

ACN: acetonitrile, DIW: deionized water, BPFITS: predicted fits.

### 2.8. Detection of Copper (II) in Real Samples

The content of copper (II) in both tap and drinking water was determined using the standard addition method. The technique included adding 500.0  $\mu\text{L}$  of CDs, 500.0  $\mu\text{L}$  of buffer ( $\text{pH} = 10.0 \pm 0.2$ ), 2 mL of DIW, and 200  $\mu\text{L}$  tap water. Varied quantities of 50-ppm copper (II) standard solution were added to achieve final copper (II) concentrations ranging from 5.21 to 25.4  $\mu\text{M}$ . The FI was measured using  $\lambda_{\text{ex}}$  of 310 nm, and the fluorescence emission intensity was measured at  $\lambda_{\text{em}}$  of 410 nm. The same procedure was repeated for

the drinking water, and recovery calculations were executed in both cases using the ‘taken’ and ‘found’ concentrations of copper (II).

### 3. Results and Discussion

#### 3.1. Optical and Structural Characterization of the Prepared CDs

##### 3.1.1. UV–Vis Spectrophotometry

The synthesized CDs were successfully dispersed in water, yielding a transparent solution. Under the UV light at 365 nm, the as-synthesized CDs exhibited a bluish fluorescence emission, as shown in the inset (Figure 1). The produced CDs solutions were analyzed using UV–vis spectra, as depicted in Figure 1. The three MBC400, 600, and 800-CDs spectra absorb in the UV region, with a weak shoulder peak between 220 and 255 nm (at 253 nm for MBC400-CDs). This shoulder may be ascribed to the  $\pi$ – $\pi^*$  transitions of the aromatic C–C and C = C bonds generated from the aromatic biochar  $\pi$ -system [46–48]. No absorption hump could be noted near 340 nm, implying the presence of a relatively broad size distribution of CDs [46].

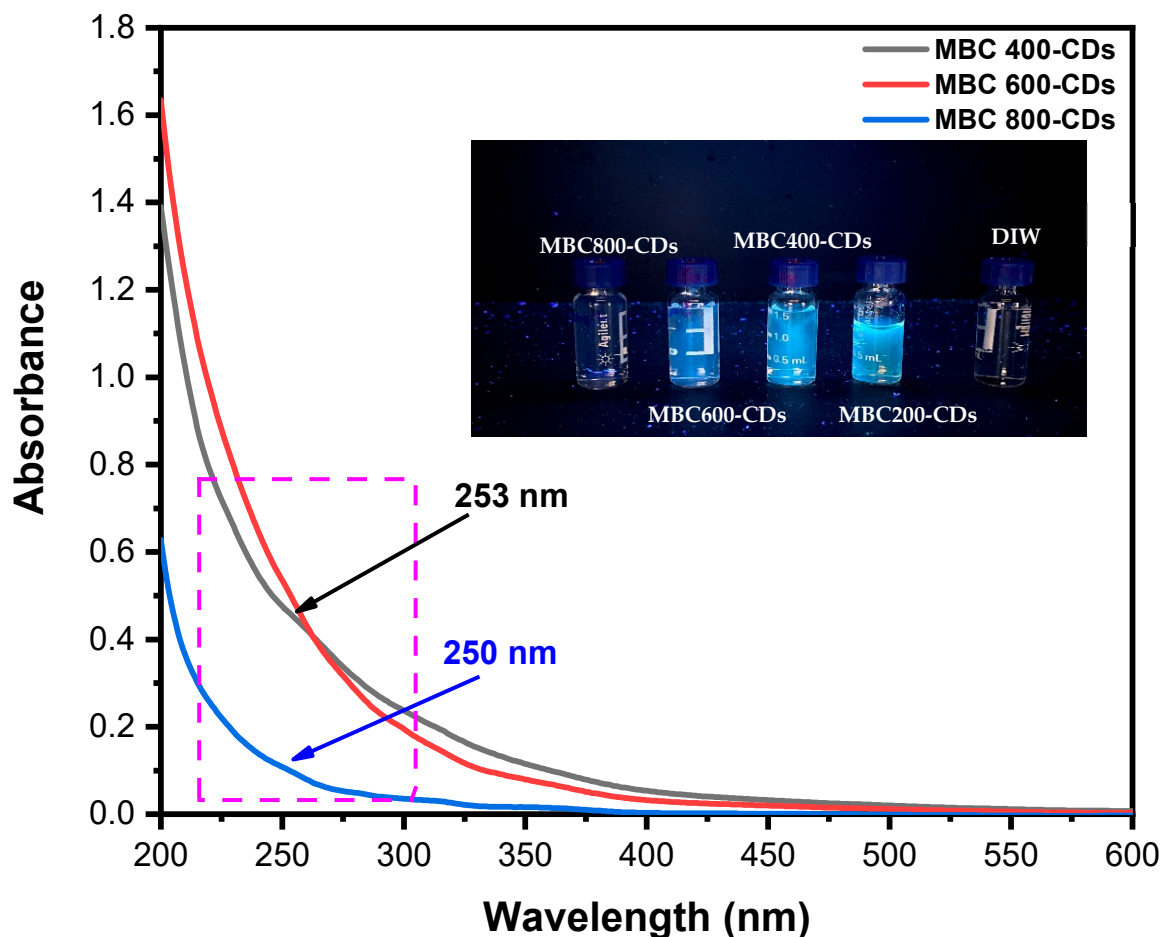


**Figure 1.** UV–vis spectra of the as-prepared MBC400, 600, and 800-CDs, including an inset image showing the CDs samples under UV light at 365 nm compared to DIW (far right).

Figure 2 shows that MBC400-CDs featured excitation-dependent fluorescence emission characteristics, allowing for wavelength adjustable emission. The red shift in emission intensity happened when the excitation wavelength was altered from 330 nm to 350 nm. The CDs were best stimulated at 310 nm, yielding the highest emission intensity. The maximum photoluminescence intensity of MBC400-CDs is centered at 410 nm.

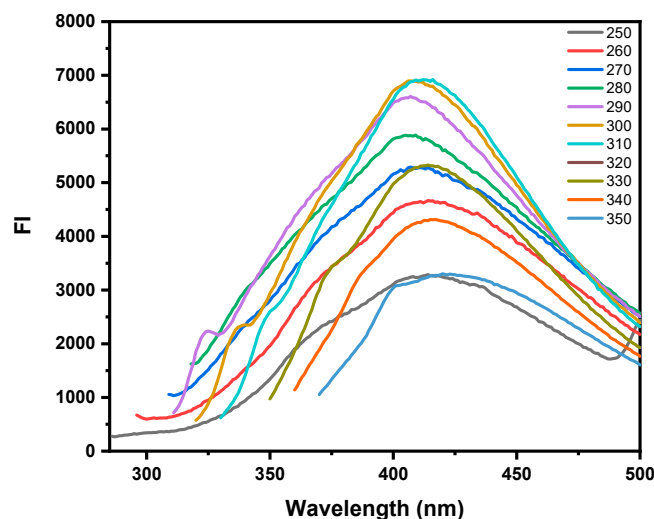


**Figure 2.** Fluorescence emission spectra of the as-synthesized MBC400-CDs emitted using different excitation wavelengths in the range between 250 and 350 nm.

### 3.1.2. Selection of the Carbon Precursor

The carbon precursor for CDs synthesis was selected after testing four biochar samples: MBC200, MBC400, MBC600, and MBC800. The CDs generated from these biochars were principally compared in terms of their quantum yield (QY%), as shown in Table 4. Among these, the MBC400-CDs showed the highest QY%, reaching 7.31%. This finding conforms with earlier research suggesting that biochar produced below 400 °C might not be fully carbonized [49]. For this reason, the MBC200-CDs were difficult to filter. Furthermore, the data indicated that as the pyrolysis temperature rose from 400 °C to 800 °C, the QY% decreased. This trend is consistent with previous studies that observed a decline in photoluminescence with higher carbonization temperatures [46]. Therefore, the MBC400-CDs sample was chosen for further investigation. A comparison between the QY% of different CDs prepared from biochar as a precursor is reported in Table 4. The comparison shows that the current CDs derived from MBC possess a quite similar QY% when matched to the reported biochar-derived CDs, as shown in Table 5.

**Table 4.** QY% of the obtained CDs compared to quinine sulfate.

Sample	Integrated Emission Intensity (I) Area	Refractive Index ( $\eta$ )	Absorbance (A) (at $\lambda_{ex} = 314 \text{ nm}$ )	QY (at $\lambda_{ex} = 314 \text{ nm}$ )
Quinine sulfate	8,051,819.586	1.33	0.052	
MBC400-CDs	$2.63 \times 10^6$		0.127	7.31%
MBC600-CDs	$2.39 \times 10^6$		0.149	5.66%
MBC800-CDs	$1.03 \times 10^5$		0.03	1.21%

**Table 5.** A comparison between the biochar-sourced CDs and the CDs synthesized in the current approach.

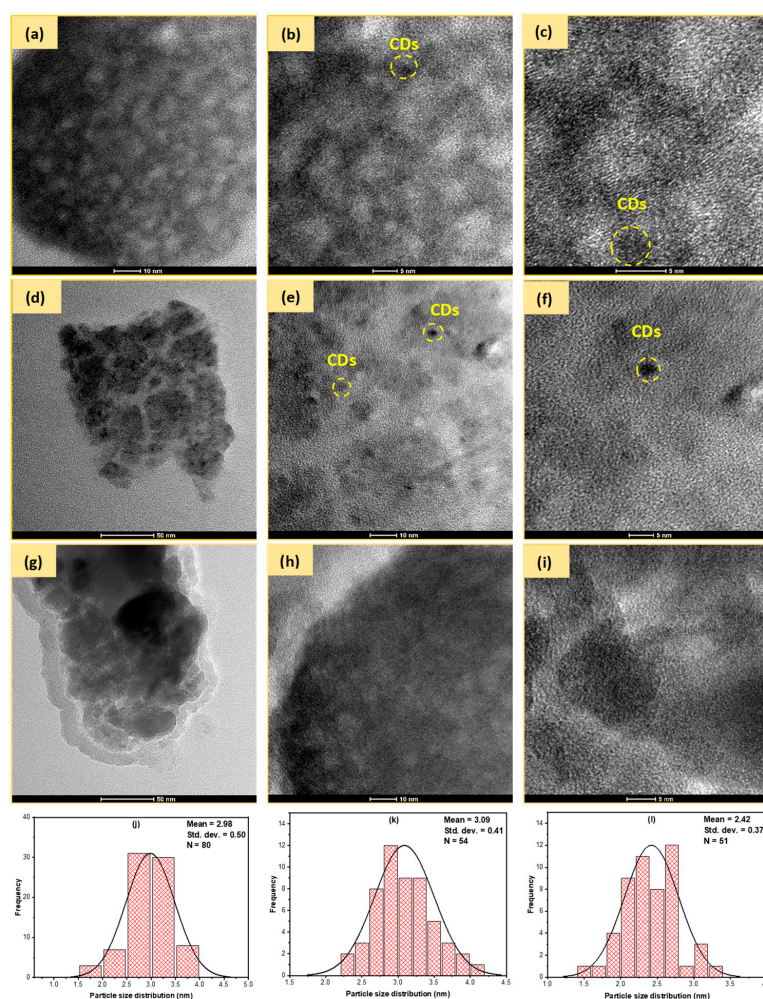
Feedstock	Pyrolysis Temperature	Synthesis	%QY	Ref.
Avocado seeds	250, 400, and 600 °C	Hydrothermal synthesis	250 °C: 9.2% 400, 600 °C: ~2–3%	[46]
Purple moor grass biochar ( <i>Molinia caerulea</i> )	300–375 °C	Hydrothermal synthesis	8.39%	[13]
Spruce tree biochar ( <i>Picea</i> )	Not stated	synthesis in the presence of $\text{KMnO}_4$	5.44%	
African oil palm biochar ( <i>Elaeis guineensis</i> )	200–400 °C		2.31%	

Table 5. Cont.

Feedstock	Pyrolysis Temperature	Synthesis	%QY	Ref.
Peanut shells	340–420 °C	Sonication	10.58%	[50]
Watermelon peels	Carbonization at low temperature	Sonication	7.1%	[51]
Mandarin peels	400, 600 and 800 °C	Hydrothermal synthesis	400 °C: 7.31% 600 °C: 5.66% 800 °C: 1.21%	This work

### 3.1.3. Transmission Electron Microscopy (TEM)

TEM pictures revealed the morphologies and particle sizes of the as-prepared CDs. As shown in Figure 3a–i, most particles possess a uniform spherical shape. The particle size distribution (PSD) (Figure 3j–l) shows that MBC400-CDs have a particle size of  $2.98 \pm 0.50$  nm, the PSD of the MBC600-CDs is  $3.09 \pm 0.41$  nm, and the MBC800-CDs had an average size of  $2.42 \pm 0.37$  nm. The MBC600-CDs sample has the largest PSD followed by MBC400-CDs, and MBC800-CDs sample has the smallest average size. The inset in Figure 3c shows the presence of tiny CDs with an inner core of 0.22 nm and an outer shell with amorphous structure which is characteristic for the CDs [52,53].



**Figure 3.** TEM micrographs of the prepared samples: (a–c) MBC400-CDs, (d–f) MBC600-CDs, and (g–i) MBC800-CDs at different scales between 5 and 50 nm. Micrographs denoted by the letters (j–l) are the PSD of the prepared samples from MBC400, 600, and 800, respectively.

### 3.1.4. Fourier Transform Infrared (FTIR) Spectroscopic Analysis

FTIR spectra were employed to explore the functional groups on the surface of the produced MBC400-CDs, Figure 4a. The FTIR absorption spectra showed a broad absorption band at  $3378\text{ cm}^{-1}$ , revealing the presence of O–H stretching vibrations mode. The broad band could be attributed to the presence of water with acidic functional groups. The two absorption bands at  $2937$  and  $2725\text{ cm}^{-1}$  revealed the presence of  $\text{CH}_2$  antisymmetric stretching vibrations and  $\text{CH}_2$  symmetric stretching vibrations, respectively [54]. A significant absorption band at  $1612\text{ cm}^{-1}$  indicates C=C stretching vibrations, confirming the presence of  $sp^2$  structures in the produced CDs [55–57]. Moreover, the peak at  $1851\text{ cm}^{-1}$  as well as at  $1652\text{ cm}^{-1}$  could indicate the presence of C=O stretching vibrations [58]. In contrast, a strong peak at  $1386\text{ cm}^{-1}$  could be ascribed to C–N stretching vibrations. The two peaks at  $1117\text{ cm}^{-1}$  and  $1007\text{ cm}^{-1}$  could be associated with aromatic C–H in-plane bending vibration. On the other hand, the absorption bands in the range between  $969$  and  $661\text{ cm}^{-1}$  show the presence of aromatic C–H out-plane bending vibrations [59,60]. The peak at  $608\text{ cm}^{-1}$  could be attributed to the vibrations originating from the aromatic carbon [61]. The obtained data confirm the aromaticity of the formed CDs with the presence of important functional groups, including C=O and C–N, which positively affect the reaction capability towards metal ions.

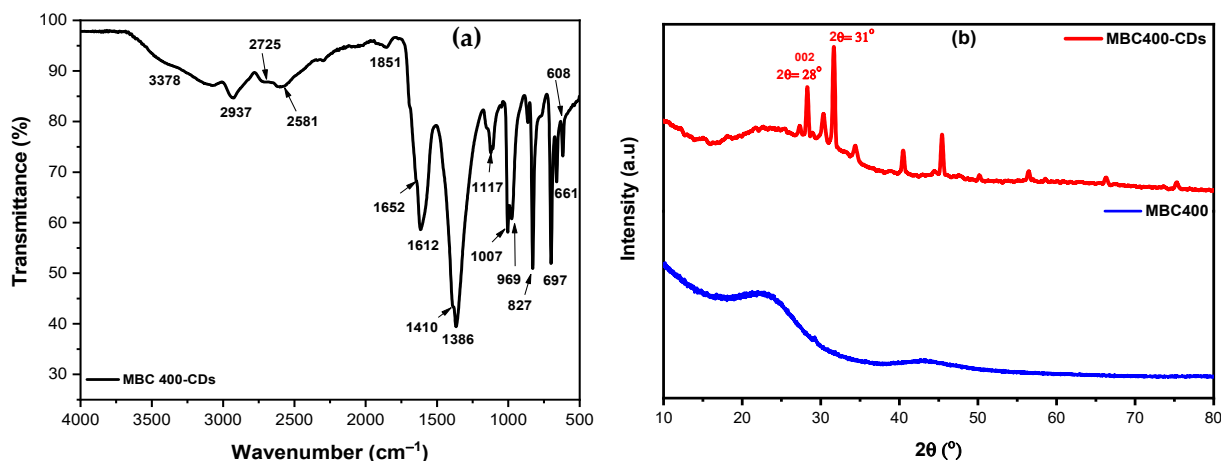


**Figure 4.** (a) FTIR spectrum of MBC400-CDs and (b) powder XRD pattern of the samples MBC400 (blue line) and MBC400-CDs (red line).

### 3.1.5. X-ray Diffraction (XRD)

The structural properties of both MBC400 and MBC400-CDs were analyzed using the X-ray Diffraction pattern (XRD) depicted in Figure 4b. The XRD pattern of MBC400 (blue line) shows the presence of a broad peak in the range between  $2\theta$ :  $17^\circ$  and  $32^\circ$ , confirming the presence of an amorphous structure of the MBC400 [62]. On the other hand, the XRD pattern of the prepared CDs (red line) shows the presence of some significant peaks compared to the parent biochar sample, including a broad and intense diffraction peak at  $2\theta = 28$  and  $31^\circ$ , corresponding to the (002) plane of carbonaceous CDs. This peak aligns with earlier structural analyses of carbon quantum dots, as documented in JCPDS Card No. 26–1076 [63,64].

### 3.1.6. Stability Testing of MBC400-CDs

The stability of the MBC400-CDs fluorescence was investigated by recording the response, FI, at different concentrations (0.2–1.0 M) of NaCl. The obtained data shown in Figure 5a reveal no changes in the fluorescence intensity of the MBC400-CDs, even when the NaCl concentration reached 1.0 M, confirming the remarkable stability of CDs under high ionic strength conditions. The photostability of the MBC400-CDs was also studied by noting the change in FI over 3 h (continuous irradiation). The collected data shown in Figure 5b

reflect the high stability of MBC400-CDs over a long period of time. Both plots confirm the stability of MBC400-CDs, with no significant decrease in the fluorescence intensity.

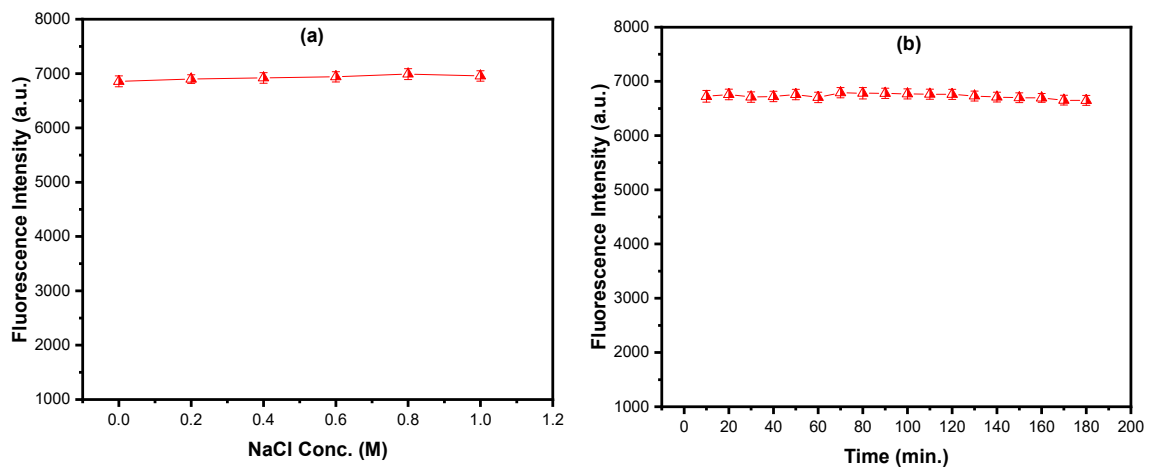
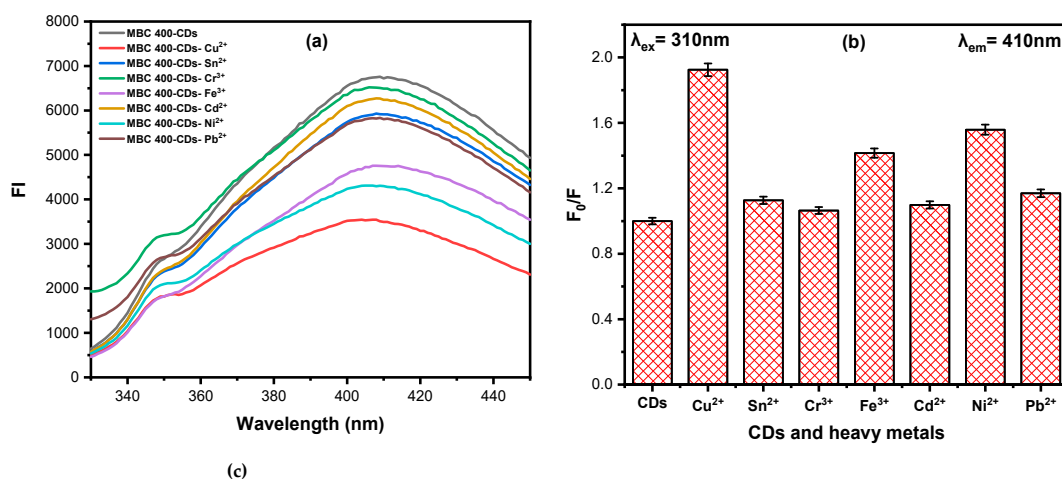


**Figure 5.** (a) The MBC400-CDs fluorescence intensity (FI) measured in different concentrations of NaCl and (b) MBC400-CDs FI measured versus time.

### 3.2. Selectivity Analysis

Figure 6a shows that the addition of various metal ions reduced the FI of MBC400-CDs to different levels. Figure 6b confirmed the quenching potential of each metal, where tin (II), chromium (III), cadmium (II) and lead (II) generated a minor quenching effect. On the other hand, iron (III) and nickel (II) produced a more noticeable effect. Copper (II) caused a significant drop in the FI, reaching a quenching percentage of 48.1% under non-optimum conditions.



(c)



**Figure 6.** (a,b) is the selectivity test of the prepared MBC 400-CDs towards different metal ions, (c) a photo showing the MBC400-CDs sample before and after quenching using different heavy metal ions under irradiation using a longer wavelength UV lamp.

Moreover, the interference of different heavy metals with copper (II) detection using MBC400-CDs was evaluated by determining the tolerance limit towards ions that caused quenching of the fluorescence of MBC400-CDs but to a lower extent compared to copper (II) ions. Tested ions included iron (III), cadmium (II), nickel (II), and chromium (III). The tolerance limit is the concentration of interfering ions that causes a deviation in the copper (II) quenching effect  $\geq 10\%$  [65]. For this purpose, the quenching effect of 25  $\mu\text{M}$  copper (II) was measured first, followed by the addition of varying concentrations of the interfering ions, ranging from 5 to 200  $\mu\text{M}$ . The tolerance limit was then calculated using Equation (3) as follows:

$$\text{Tolerance limit} = \left| \frac{F_0 - F}{F_0} \right| \times 100 \quad (3)$$

In this formula,  $F_0$  is the fluorescence intensity of MBC400-CDs in the presence of 25  $\mu\text{M}$  copper (II) solution measured at the optimum conditions, and  $F$  is the fluorescence intensity after the addition of the interferent ion. The obtained data shown in Table 6 reveal that the tolerance limit was lower than 10% for iron (III) (1.05–7.41%), chromium (III) (0.21–3.14%), and cadmium (II) (0.17–3.04%) at all tested concentrations, implying that the existence of these interferent ions has a slight effect on the detection of copper (II) using MBC400-CDs. In contrast, nickel (II) shows a higher deviation, particularly at concentrations  $> 100 \mu\text{M}$ , suggesting that concentrations of nickel (II) below 100  $\mu\text{M}$  do not interfere with copper (II) detection using the current approach. These findings demonstrate that the proposed method provides excellent selectivity for copper (II) detection even with the co-existence of various interfering metal ions.

**Table 6.** Effect of different metal ions on MBC400-CDs–copper (II) fluorescence and the calculated tolerance limit.

Concentration of the Interferent Metal Ion ( $\mu\text{M}$ )	Tolerance Limit			
	Iron (III)	Nickel (II)	Chromium (III)	Cadmium (II)
5	1.05	1.26	0.21	0.17
10	1.43	2.69	0.38	0.33
20	2.19	3.88	0.72	0.59
40	2.79	6.38	1.32	1.19
60	3.48	8.22	1.59	1.51
80	4.03	9.03	1.72	1.68
100	4.27	10.07	2.17	1.94
150	5.79	13.13	2.63	2.51
200	7.41	16.08	3.14	3.04

### 3.3. Screening of Variables Affecting Copper (II) Detection

In this work, PBD was utilized to describe the association between three independent variables (CT, pH, and RM) and the dependent response ( $F_0/F$ ). The experimental data was fitted using the polynomial equation given in Equation (4).

The Box–Cox response transformation with a transformation factor,  $\lambda = -1$ , yielded the following regression equation:

$$\frac{-F}{F_0} = -0.9377 + 0.03309 \text{ pH} + 0.001836 \text{ Time} + 0.02355 \text{ RM} - 0.04487 \text{ Ct Pt} \quad (4)$$

Ct Pt denotes the central point in the regression model defined by Equation (4). According to this model, all analyzed variables had a positive impact on the response, with pH having the highest effect. The suggested model's reliability was further supported by the  $R^2$  (0.9544) and adjusted  $R^2$  (0.9485) values, which demonstrate a good correlation between experimental and model-predicted values. Also, the expected  $R^2$  was a higher value (0.9388), demonstrating the model's ability for predicting every additional observation.

The Pareto chart, Figure 7a, depicts the relationship between the response,  $F_0/F$ , and the three factors. As demonstrated, all variables exceeded the reference line, indicating their statistical significance with pH (A) being the most statistically significant.

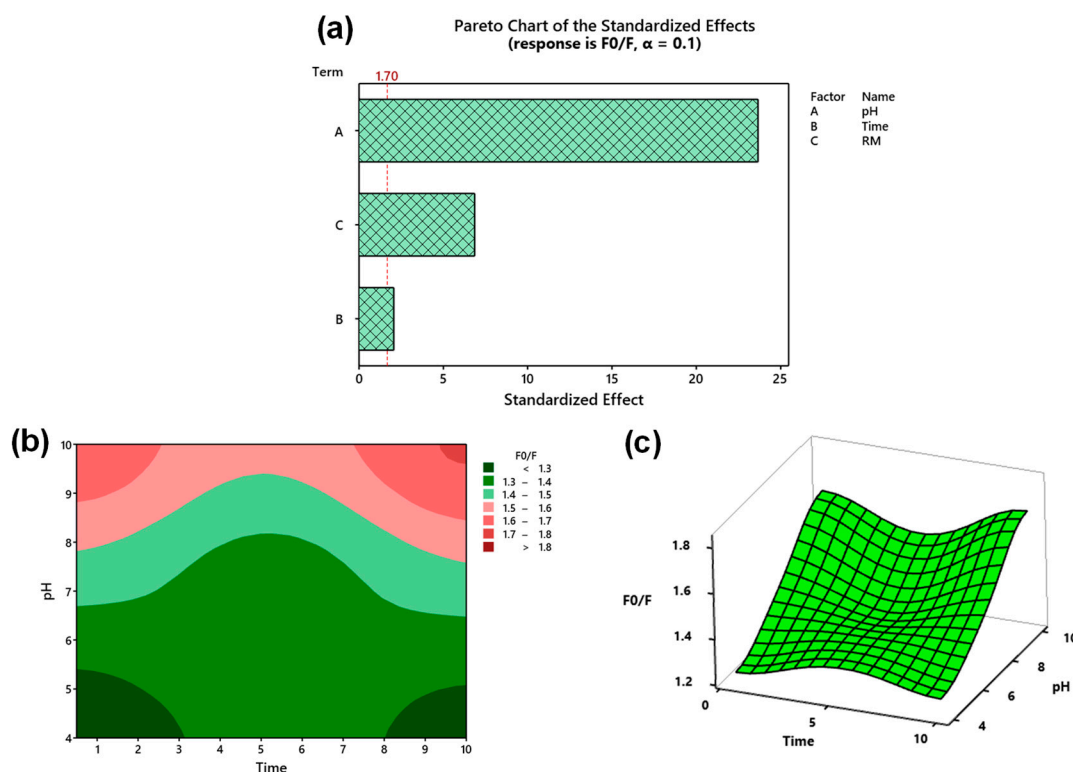


**Figure 7.** (a) Pareto chart of standardized effects, (b) 2D contour plots, and (c) 3D surface plots for pH and CT.

The 2D contour plots shown in Figure 7b were used to study the relationship between the response variable and two predictor variables, which are shown along the x- and y-axes. The x- and y-axes in Figure 7b indicate the two numerical variables, Time (C) and pH(A), respectively. The dark green contours represent an area where fluorescence quenching is lowest, with pH ranging from 4 to 5.4 and Time between  $\approx 0$  and 3 min and  $\approx 8$  and 10 min. The 3D surface plots were used to measure the relationship between the same two variables, but in a 3D format, with the z-axis representing the response variable. As illustrated in Figure 7c, the high ridges suggest that fluorescence quenching can be increased at both high pH (pH = 10) and Time (10 min). Analysis of variance (ANOVA) showed that all variables have a  $p$ -value  $< 0.05$ , confirming their statistical significance. The lack-of-fit showed a  $p$ -value that is greater than 0.05, implying insignificant lack-of-fit and hence good model linearity.

The individual desirability function ( $d$ ) was used to determine the optimal experimental conditions that could simultaneously maximize the response variable. The desirability plot revealed that the highest fluorescence quenching could be reached by combining Time of 10 min, pH of 10, and using DIW as the RM. These best conditions were then used to generate the calibration curve and apply the standard addition approach.

The CDs' surface charge could explain why the ideal pH was at a higher value. Under low pH conditions (acidic pH), the functional moieties such as carboxyl groups and other oxygenated moieties on the surface of CDs become protonated, resulting in a highly positively charged surface. This phenomenon causes the positively charged copper (II) to be repelled from the surface of the CDs. As a result, fluorescence quenching triggered by existence of copper (II) could be inefficient at low pH levels. When the pH rises, the

functional groups on the surface of the CDs gradually deprotonate, allowing the interaction between the negatively charged surface and the copper (II) cations [65–67].

### 3.4. Method Validation

#### 3.4.1. Calibration Curve: Linear Range and Sensitivity

The calibration curve obtained for detecting copper (II) using MBC400-CDs showed that as the concentration of copper (II) increased within the range of 4.9–56.6  $\mu\text{M}$  and 56.6–197.5  $\mu\text{M}$ , there was a consistent linear correlation between the concentration of copper (II) and the response,  $F_0 - F/F$ . This change was measured using excitation and emission wavelengths of 310 and 410 nm, respectively. Equations (5) and (6) represent this linear correlation.

$$y = 0.3966x + 9.5312, \quad R^2 = 0.9971 \quad (5)$$

$$y = 0.211x + 21.945, \quad R^2 = 0.9879 \quad (6)$$

where  $y$  indicates the response  $F_0 - F/F$ , and  $x$  is the concentration of copper (II). The high coefficient of determination,  $R^2$ , suggests that the data exhibited strong linearity. Figure 8a shows the calibration curve for different concentrations of copper (II), determined using MBC400-CDs under the optimal experimental conditions. The fluorescence spectra of MBC400-CDs before and after adding different concentrations of copper (II) is shown in Figure 8b.

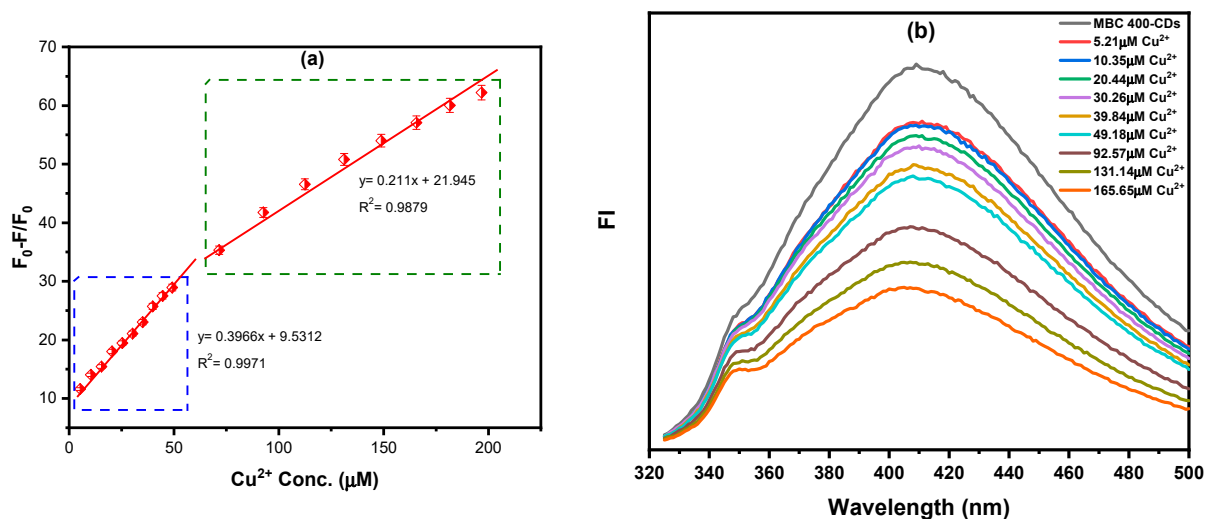


**Figure 8.** (a) The calibration curve for different concentrations of copper (II), determined using MBC400-CDs. (b) Fluorescence spectra of MBC400-CDs before and after adding different concentrations of copper (II).

To assess the sensitivity of the proposed approach, the limit of detection (LOD) and limit of quantification (LOQ) were calculated operating the formulas in Equations (7) and (8), correspondingly, and using the values of the standard deviation ( $\sigma$ ) of the blank sample, and the slope ( $s$ ) of the linear calibration curve (first linear segment).

$$LOD = 3 \times \frac{\sigma}{s} \quad (7)$$

$$LOQ = 10 \times \frac{\sigma}{s} \quad (8)$$

For a linear range of 4.9–56.6  $\mu\text{M}$ , the LOD is 0.01  $\mu\text{M}$ , and the LOQ is 0.04  $\mu\text{M}$ . These results highlight the remarkable sensitivity of the produced MBC400-CDs towards copper (II). The allowable level of copper in drinking water is 1.3 mg/L, which is approximately 20.5  $\mu\text{M}$ . This value is significantly greater than our reported LOD (0.01  $\mu\text{M}$ ). In other

words, the synthesized MBC400-CDs could detect copper (II) concentrations much below the allowable limit, making them useful candidates for environmental monitoring purposes. Furthermore, Table 7 shows a comparison of the performance of the mandarin peel-derived CDs with the other reported CD-based approaches for detecting copper (II). The comparison included both greenly [68–73] and chemically [74–77] synthesized CDs. As can be seen from Table 7, the mandarin peel biochar-derived CDs were working effectively over a wide concentration range. Moreover, comparing the performance of MBC400-CDs to the greenly synthesized CDs [68–73] revealed a reasonable LOD that is lower than the reported approaches. The LOD was also lower than the reported values using GQDs [76] and CDs derived from the pyrolysis of mixture of citric acid, sodium borohydride, and polyethyleneimine [77]. The NCDs (derived from urea and ethylenediaminetetraacetic acid) [74] and the CA-CdS QDs (obtained from citric acid, cadmium chloride, and thioacetamide) [75] showed a lower LOD; however, the procedure involved usage of hazardous chemicals at higher temperatures. The QY% is comparable to and sometimes higher than the reported CD-based sensors of green origin. Compared to the CDs from chemicals, the %QY of MBC400-CDs was lower; however, the current approach does not entail the use of any surface passivation, chemical modification, or doping. None of the reported approaches have employed a factorial design to control the variables affecting the sensing rehearsal.

**Table 7.** A comparison between different CD-based fluorescence sensors and the current approach for detecting copper (II).

Probe	Synthesis Method	Green Synthesis	Controlled Sensing	Linear Range	LOD	QY	Reference
BPEI-CQDs	Hydrothermal conversion of bamboo leaves at 200 °C followed by capping with branched polyethylenimine	Yes	No	1–140 µM	0.01 µM	7.1%	[68]
CQDs	Microwave-assisted carbonization of empty fruit bunch at 60–100 °C	Yes	No	0–400 µM	0.42 µM	Not stated	[69]
CDs <sub>100–180</sub>	Hydrothermal carbonization of biomass (hemicelluloses, lignin, chitosan, and α-cellulose) at 100–180 °C	Yes	No	0–30 µM	0.085 µM	2.8–16.6%	[70]
CNDs (nitrogen containing)	Hydrothermal treatment of pipe tobacco	Yes	No	0–40 µM	0.01 µM	3.2%	[71]
CQDs	Carbonization of petals of <i>Polianthes tuberosa</i> L. at 300 °C for 8 h	Yes	No	0–70 µM	0.2 µM	3%	[72]
NCDs	Thermal coupling of lemon extracts and L-arginine at 200 °C for 3 h	Yes	No	0.05–300 µM	0.047 µM	7.7%	[73]
NCDs	Pyrolysis of urea and ethylenediaminetetraacetic acid at 200–300 °C for 1 h	No	No	0.001–22 µM	0.002 µM	11.26%	[74]
CA-CdS QDs	Hydrothermal synthesis from cadmium chloride and thioacetamide, using citric acid for surface modification	No	No	0.01–50 µM	0.009 µM	18.82%	[75]
GQDs	Hydrothermal method at 180 °C for 10 h from graphene oxide (reoxidized in mixture of concentrated sulfuric and nitric acids)	No	No	0–15 µM	0.226 µM	Not stated	[76]

Table 7. Cont.

Probe	Synthesis Method	Green Synthesis	Controlled Sensing	Linear Range	LOD	QY	Reference
CDs	Pyrolysis of mixture of citric acid, sodium borohydride, and polyethyleneimine at 180 °C for 1 h in an oil bath	No	No	0–80 µM	5.3 µM	25%	[77]
MBC400-CDs	Hydrothermal synthesis using renewable source, mandarin peels, at 180 °C for 4 h	Yes	Yes	4.9–56.6 µM 56.6–197.5 µM	0.01 µM	7.31%	This work

BPEI: branched polyethyleneimine; CDs<sub>100–180</sub>: CDs prepared at temperatures from 100 to 180 °C, CNDs: Carbon nanodots; NCDs: nitrogen-doped carbon dots; CA-CdS QDs: citric acid-capped CdS quantum dots; GQDs: graphene quantum dots.

### 3.4.2. Accuracy and Precision

The accuracy and precision of the proposed procedure in the authentic samples were measured at a 95.0% confidence interval (95.0% CI), as shown in Table 8. The acquired data demonstrated a % mean recovery of  $100.3 \pm 3.2$ , validating the accuracy of the suggested approach. The % relative standard deviation was less than 5%, implying a high precision of the proposed procedure.

Table 8. Detection of copper (II) in authentic samples.

Taken (µM)	Found (µM)	% Recovery
5.21	5.27	101
10.4	10.8	104
15.4	14.9	96.8
20.4	21.4	105
25.4	25.0	98.4
30.3	29.1	96.0
35.1	34.0	96.9
39.8	40.8	103
44.5	45.4	102
49.2	48.9	99.4
Mean ± SD		100.3 ± 3.2
% RSD		3.2

### 3.4.3. Analysis of Real Samples

For real samples, the accuracy was tested using recovery studies after spiking the real samples with standard copper (II) solution, as shown in Table 9. Copper (II) recovery rates were  $104 \pm 0.85\%$  in tap water compared to  $102 \pm 1.45\%$  in the case of mountain water (Table 9), suggesting a good accuracy. These good results indicate that the matrix, which frequently contains other interfering components, has only a minor impact on the current sensor's ability to detect copper (II).

Table 9. The concentration of copper (II) spiked in tap and mountain waters, as detected by the MBC400-CDs.

Sample	Copper (II)			
	Spiked (µM)	Found (µM)	Recovery%	RSD%
Tap water	0	2.43	-	0.78
	5.21	5.29	102	0.97
	10.4	11.1	107	1.28
	15.4	16.2	105	0.96
	20.4	21.3	104	0.68
	25.4	25.6	101	0.36

Table 9. Cont.

Sample	Copper (II)			
	Spiked ( $\mu\text{M}$ )	Found ( $\mu\text{M}$ )	Recovery%	RSD%
Mountain water	0	11.9	-	2.01
	5.21	5.34	102	1.29
	10.3	10.4	100	2.06
	15.4	15.7	102	2.01
	20.4	21.4	105	0.94
	25.4	25.6	101	0.36

### 3.5. Proposed Quenching Mechanism

Under UV irradiation at 310 nm, the CDs emit a strong fluorescence at 410 nm, resulting from electron excitation from the valence band (VB) to the conduction band (CB). With the addition of copper (II) to the CD solution, they interact with negatively charged functional groups on the surface of the CDs. This electrostatic interaction facilitates the splitting of the copper (II) *d* orbital energy levels, providing an alternative pathway for electron transfer. In this process, electrons from the excited state in the CB of the CDs transfer to the *d* orbitals of the copper (II) ions. The electrons were then returned to the ground state, bypassing the normal fluorescence pathway of the CDs. This electron transfer significantly reduces the fluorescence emission as the energy disruption alters the electronic transitions within the CDs, resulting in a quenching effect [78–80]. The degree of quenching is proportional to the concentration of copper (II) ions, making MBC400-CDs highly useful for detecting copper (II) in solutions with great sensitivity [77,81].

## 4. Conclusions

In conclusion, this study reports the green synthesis of carbon dots (CDs) derived from mandarin peel biochar (MBC) prepared at various pyrolysis temperatures. The CDs synthesized from MBC pyrolyzed at 400 °C (MBC400-CDs) exhibited remarkable luminescent properties, with a high quantum yield (QY) of 7.31%. The formed CDs at 400 °C showed small particles of  $2.98 \pm 0.50$  nm, as confirmed by the TEM analysis. The MBC400-CDs showed strong emission intensity, with optimal excitation at 310 nm. After optimization of the experimental conditions affecting the sensing process using PBD, an ON–OFF copper (II) sensing system was established. The developed system showed a rapid response and reasonable selectivity with high sensitivity (a detection limit as low as 0.01  $\mu\text{M}$ ) over a wide linear response range (4.9–197.5  $\mu\text{M}$ ). Method validation confirmed the high accuracy and precision. The MBC400-CDs also showed exceptional performance in measuring copper (II) concentrations in real water samples, as reflected by the high precision and recoveries. The analytical technique developed in the current investigation has therefore demonstrated the potential of biochar-derived CDs for environmental applications.

**Author Contributions:** Conceptualization, M.E.-A., A.S.E.-S. and K.A.-S.; methodology, M.E.-A., A.S.E.-S., A.A. (Abdulrahman Alahzm) and A.A. (Alaa AlReyashi); software, M.E.-A., A.S.E.-S. and A.A. (Alaa AlReyashi); validation, M.E.-A., A.S.E.-S., N.A.-H., K.A.-S. and M.A.A.-G.; formal analysis, M.E.-A. and A.S.E.-S.; investigation, M.E.-A., A.S.E.-S. and A.A. (Abdulrahman Alahzm); resources, M.E.-A., A.S.E.-S. and K.A.-S.; data curation, M.E.-A., A.S.E.-S. and A.A. (Alaa AlReyashi); writing—original draft preparation, M.E.-A., A.S.E.-S. and A.A. (Alaa AlReyashi); writing—review and editing, M.E.-A., A.S.E.-S. and A.A. (Alaa AlReyashi); visualization, M.E.-A., A.S.E.-S. and A.A. (Alaa AlReyashi); supervision, M.E.-A.; project administration, M.E.-A., A.S.E.-S., K.A.-S., N.A.-H., M.A.A.-G. and M.F.S.; funding acquisition, M.E.-A., A.S.E.-S., N.A.-H., K.A.-S., M.F.S. and M.A.A.-G. All authors have read and agreed to the published version of the manuscript.

**Funding:** This publication was supported by the Qatar University Collaborative Grant [QUCG-CAS-23/24-234]. The findings achieved herein are solely the responsibility of the authors.

**Data Availability Statement:** Data are contained within the article.

**Acknowledgments:** The work members would like to extend their special thanks to the Central Lab Unit (CLU) at Qatar University.

**Conflicts of Interest:** The authors declare no conflicts of interest.

## References

1. Shabbir, H.; Csapó, E.; Wojnicki, M. Carbon Quantum Dots: The Role of Surface Functional Groups and Proposed Mechanisms for Metal Ion Sensing. *Inorganics* **2023**, *11*, 262. [CrossRef]
2. Sharma, A.; Choi, H.K.; Lee, H.J. Carbon Dots for the Treatment of Inflammatory Diseases: An Appraisal of In Vitro and In Vivo Studies. *Oxidative Med. Cell. Longev.* **2023**, *2023*, 3076119. [CrossRef]
3. Sharma, V.; Tiwari, P.; Kaur, N.; Mobin, S.M. Optical nanosensors based on fluorescent carbon dots for the detection of water contaminants: A review. *Environ. Chem. Lett.* **2021**, *19*, 3229–3241. [CrossRef]
4. Stepanidenko, E.A.; Vedernikova, A.A.; Badrieva, Z.F.; Brui, E.A.; Ondar, S.O.; Miruschenko, M.D.; Volina, O.V.; Koroleva, A.V.; Zhizhin, E.V.; Ushakova, E.V. Manganese-Doped Carbon Dots as a Promising Nanoprobe for Luminescent and Magnetic Resonance Imaging. *Photonics* **2023**, *10*, 757. [CrossRef]
5. El-Azazy, M.; Osman, A.I.; Nasr, M.; Ibrahim, Y.; Al-Hashimi, N.; Al-Saad, K.; Al-Ghouti, M.A.; Shibl, M.F.; Ala'a, H.; Rooney, D.W. The interface of machine learning and carbon quantum dots: From coordinated innovative synthesis to practical application in water control and electrochemistry. *Coord. Chem. Rev.* **2024**, *517*, 215976. [CrossRef]
6. Bhakare, M.A.; Bondarde, M.P.; Lokhande, K.D.; Dhumal, P.S.; Some, S. Quick transformation of polymeric waste into high valuable N-self doped carbon quantum dot for detection of heavy metals from wastewater. *Chem. Eng. Sci.* **2023**, *281*, 119150. [CrossRef]
7. Dhandapani, E.; Maadeswaran, P.; Raj, R.M.; Raj, V.; Kandiah, K.; Duraisamy, N. A potential forecast of carbon quantum dots (CQDs) as an ultrasensitive and selective fluorescence probe for Hg (II) ions sensing. *Mater. Sci. Eng. B* **2023**, *287*, 116098. [CrossRef]
8. Chaghghazardi, M.; Kashanian, S.; Nazari, M.; Omidfar, K.; Joseph, Y.; Rahimi, P. Nitrogen and sulfur co-doped carbon quantum dots fluorescence quenching assay for detection of mercury (II). *Spectrochim. Acta Part A Mol. Biomol. Spectrosc.* **2023**, *293*, 122448. [CrossRef]
9. Shao, N.; Jin, J.; Wang, H.; Zheng, J.; Yang, R.; Chan, W.; Abliz, Z. Design of bis-spiropyran ligands as dipolar molecule receptors and application to in vivo glutathione fluorescent probes. *J. Am. Chem. Soc.* **2010**, *132*, 725–736. [CrossRef]
10. van Dijk, M.A.; Kapitein, L.C.; van Mameren, J.; Schmidt, C.F.; Peterman, E.J. Combining optical trapping and single-molecule fluorescence spectroscopy: Enhanced photobleaching of fluorophores. *J. Phys. Chem. B* **2004**, *108*, 6479–6484. [CrossRef]
11. Meng, W.; Bai, X.; Wang, B.; Liu, Z.; Lu, S.; Yang, B. Biomass-Derived Carbon Dots and Their Applications. *Energy Environ. Mater.* **2019**, *2*, 172–192. [CrossRef]
12. Fang, M.; Wang, B.; Qu, X.; Li, S.; Huang, J.; Li, J.; Lu, S.; Zhou, N. State-of-the-art of biomass-derived carbon dots: Preparation, properties, and applications. *Chin. Chem. Lett.* **2024**, *35*, 108423. [CrossRef]
13. Barrientos, K.; Gaviria, M.I.; Arango, J.P.; Placido, J.; Bustamante, S.; Londoño, M.E.; Jaramillo, M. Synthesis, characterization and ecotoxicity evaluation of biochar-derived carbon dots from Spruce tree, Purple moor-grass and African oil palm. *Processes* **2021**, *9*, 1095. [CrossRef]
14. Singh, P.; Arpita, Kumar, S.; Kumar, P.; Kataria, N.; Bhankar, V.; Kumar, K.; Kumar, R.; Hsieh, C.-T.; Khoo, K.S. Assessment of biomass-derived carbon dots as highly sensitive and selective templates for the sensing of hazardous ions. *Nanoscale* **2023**, *15*, 16241–16267. [CrossRef]
15. El-Azazy, M.; El-Shafie, A.S.; Fawzy, S.; Rooney, D.W.; Osman, A.I. Competitive adsorptive removal of promazine and prometazine from wastewater using olive tree pruning biochar: Operational parameters, kinetics, and equilibrium investigations. *Environ. Sci. Pollut. Res.* **2023**, *30*, 82387–82405. [CrossRef]
16. El-Shafie, A.S.; Mahmoud, R.; Ahsan, I.; Hamdi, H.; Shibl, M.F.; El-Azazy, M. Removal of antibiotics from aqueous solutions: Insights of competitive adsorption onto Ni-impregnated biochar of spent coffee grounds. *Appl. Water Sci.* **2024**, *14*, 209. [CrossRef]
17. El-Shafie, A.S.; Abouseada, M.; El-Azazy, M. TiO<sub>2</sub>-functionalized biochar from pistachio nutshells: Adsorptive removal and photocatalytic decolorization of methyl orange. *Appl. Water Sci.* **2023**, *13*, 227. [CrossRef]
18. Lo Bello, G.; Bartoli, M.; Giorcelli, M.; Rovere, M.; Tagliaferro, A. A review on the use of biochar derived carbon quantum dots production for sensing applications. *Chemosensors* **2022**, *10*, 117. [CrossRef]
19. Plácido, J.; Bustamante-López, S.; Meissner, K.; Kelly, D.; Kelly, S. Microalgae biochar-derived carbon dots and their application in heavy metal sensing in aqueous systems. *Sci. Total Environ.* **2019**, *656*, 531–539. [CrossRef]
20. Tan, J.; Zhou, L. Two birds with one stone: One-pot hydrothermal treatment of dragon fruit peel to simultaneously prepare efficient biochar adsorbent and fluorescent carbon quantum dots. *Ind. Crops Prod.* **2024**, *210*, 118086. [CrossRef]
21. Osman, A.I.; Fawzy, S.; Farghali, M.; El-Azazy, M.; Elgarahy, A.M.; Fahim, R.A.; Maksoud, M.A.; Ajlan, A.A.; Yousry, M.; Saleem, Y. Biochar for agronomy, animal farming, anaerobic digestion, composting, water treatment, soil remediation, construction, energy storage, and carbon sequestration: A review. *Environ. Chem. Lett.* **2022**, *20*, 2385–2485.
22. Johny, A.; Pinto da Silva, L.; Pereira, C.M.; Esteves da Silva, J.C.G. Sustainability Assessment of Highly Fluorescent Carbon Dots Derived from Eucalyptus Leaves. *Environments* **2024**, *11*, 6. [CrossRef]

23. Wang, L.; Weng, S.; Su, S.; Wang, W. Progress on the luminescence mechanism and application of carbon quantum dots based on biomass synthesis. *RSC Adv.* **2023**, *13*, 19173–19194. [CrossRef]
24. Olla, C.; Cappai, A.; Porcu, S.; Stagi, L.; Fantauzzi, M.; Casula, M.F.; Mocci, F.; Corpino, R.; Chiriu, D.; Ricci, P.C.; et al. Exploring the Impact of Nitrogen Doping on the Optical Properties of Carbon Dots Synthesized from Citric Acid. *Nanomaterials* **2023**, *13*, 1344. [CrossRef]
25. Ludmerczki, R.; Mura, S.; Carbonaro, C.M.; Mandity, I.M.; Carraro, M.; Senes, N.; Garroni, S.; Granozzi, G.; Calvillo, L.; Marras, S.; et al. Carbon Dots from Citric Acid and its Intermediates Formed by Thermal Decomposition. *Chem.—A Eur. J.* **2019**, *25*, 11963–11974. [CrossRef]
26. Fiori, F.; Moukham, H.; Olla, F.; Piras, D.; Ledda, S.; Salis, A.; Stagi, L.; Malfatti, L.; Innocenzi, P. Highly Photostable Carbon Dots from Citric Acid for Bioimaging. *Materials* **2022**, *15*, 2395. [CrossRef]
27. Vishnukumar, P.; Sankaranarayanan, S.; Hariram, M.; Vivekanandhan, S.; Navia, R. Carbon Dots from Renewable Resources: A Review on Precursor Choices and Potential Applications. In *Green Nanomaterials: Processing, Properties, and Applications*; Ahmed, S., Ali, W., Eds.; Springer Singapore: Singapore, 2020; pp. 159–208.
28. Meiling, T. Development of a Reliable and Environmentally Friendly Synthesis for Fluorescence Carbon Nanodots.—Preparation and Characterisation of Excellent and Well-Defined Carbon Nanodots by a Fast, Simple and Cost-Efficient Synthesis Method; With Special Focus on Future Exploration and Large Scale Applications. Ph.D. Thesis, Universität Potsdam, Potsdam, Germany, 2017.
29. Kharangarh, P.R.; Ravindra, N.M.; Singh, G.; Umapathy, S. Synthesis of luminescent graphene quantum dots from biomass waste materials for energy-related applications—An overview. *Energy Storage* **2023**, *5*, e390. [CrossRef]
30. Abbas, A.; Liang, Q.; Abbas, S.; Liaqat, M.; Rubab, S.; Tabish, T.A. Eco-Friendly Sustainable Synthesis of Graphene Quantum Dots from Biowaste as a Highly Selective Sensor. *Nanomaterials* **2022**, *12*, 3696. [CrossRef]
31. Manikandan, V.; Lee, N.Y. Green synthesis of carbon quantum dots and their environmental applications. *Environ. Res.* **2022**, *212*, 113283. [CrossRef]
32. Zhang, J.; Xia, A.; Zhu, X.; Huang, Y.; Zhu, X.; Liao, Q. Co-production of carbon quantum dots and biofuels via hydrothermal conversion of biomass. *Fuel Process. Technol.* **2022**, *232*, 107276. [CrossRef]
33. Kaur, G.; Verma, N. Colorimetric determination of Cu<sup>2+</sup> ions in water and milk by apo-tyrosinase disc. *Sens. Actuators B Chem.* **2018**, *263*, 524–532. [CrossRef]
34. Zhao, W.; Jia, W.; Sun, M.; Liu, X.; Zhang, Q.; Zong, C.; Qu, J.; Gai, H. Colorimetric detection of Cu<sup>2+</sup> by surface coordination complexes of polyethyleneimine-capped Au nanoparticles. *Sens. Actuators B Chem.* **2016**, *223*, 411–416. [CrossRef]
35. Vopálenská, I.; Váchová, L.; Palková, Z. New biosensor for detection of copper ions in water based on immobilized genetically modified yeast cells. *Biosens. Bioelectron.* **2015**, *72*, 160–167. [CrossRef]
36. Brinkmann, P.; Köllner, N.; Merk, S.; Beitz, T.; Altenberger, U.; Löhmannsröben, H.-G. Comparison of Handheld and Echelle Spectrometer to Assess Copper in Ores by Means of Laser-Induced Breakdown Spectroscopy (LIBS). *Minerals* **2023**, *13*, 113. [CrossRef]
37. Pavlidis, G.; Karasali, H.; Balayiannis, G.P. Rapid and Robust Analytical Method for the Determination of Copper Content in Commercial Pesticides and Antifouling Biocides. *Environ. Process.* **2023**, *10*, 19. [CrossRef]
38. Saran, R. (Ed.) Inductively Coupled Argon Plasma Mass Spectrometry (ICP MS). In *Analytical Techniques for Trace Elements in Geochemical Exploration*; The Royal Society of Chemistry: London, UK, 2022.
39. Parsons, P.J. Atomic Spectrometry in Clinical Chemistry. In *Encyclopedia of Analytical Chemistry*; John Wiley & Sons, Ltd.: Hoboken, NJ, USA, 2006.
40. EPA. National Primary Drinking Water Regulations. Available online: <https://www.epa.gov/ground-water-and-drinking-water/national-primary-drinking-water-regulations> (accessed on 1 March 2024).
41. Woods, B.; McCurdy, E. ICP-MS: Key Steps to Control Contamination and Achieve Low Detection Limits. *Spectroscopy* **2022**, *37*, 54–56. [CrossRef]
42. El-Shafie, A.S.; Barah, F.G.; Abouseada, M.; El-Azazy, M. Performance of Pristine versus Magnetized Orange Peels Biochar Adapted to Adsorptive Removal of Daunorubicin: Eco-Structuring, Kinetics and Equilibrium Studies. *Nanomaterials* **2023**, *13*, 1444. [CrossRef]
43. El-Shafie, A.S.; Yousef, A.; El-Azazy, M. Application of Plackett–Burman Design for Spectrochemical Determination of the Last-Resort Antibiotic, Tigecycline, in Pure Form and in Pharmaceuticals: Investigation of Thermodynamics and Kinetics. *Pharmaceuticals* **2022**, *15*, 888. [CrossRef]
44. Abdulsatar Esmail, L.; Sanaan Jabbar, H. Violuric acid carbon dots as a highly fluorescence probe for ultrasensitive determination of Zn (II) in tomato paste. *Food Chem.* **2023**, *413*, 135638. [CrossRef]
45. Aly, H.; El-Shafie, A.S.; El-Azazy, M. Utilization of 7-chloro-4-nitrobenzo-2-oxa-1,3-diazole (NBD-Cl) for spectrochemical determination of l-ornithine: A multivariate optimization-assisted approach. *RSC Adv.* **2019**, *9*, 22106–22115. [CrossRef]
46. Mejía Ávila, J.; Rangel Ayala, M.; Kumar, Y.; Pérez-Tijerina, E.; Robles, M.A.R.; Agarwal, V. Avocado seeds derived carbon dots for highly sensitive Cu (II)/Cr (VI) detection and copper (II) removal via flocculation. *Chem. Eng. J.* **2022**, *446*, 137171. [CrossRef]
47. Dager, A.; Uchida, T.; Maekawa, T.; Tachibana, M. Synthesis and characterization of Mono-disperse Carbon Quantum Dots from Fennel Seeds: Photoluminescence analysis using Machine Learning. *Sci. Rep.* **2019**, *9*, 14004. [CrossRef]

48. Liu, G.; Jia, H.; Li, N.; Li, X.; Yu, Z.; Wang, J.; Song, Y. High-fluorescent carbon dots (CDs) originated from China grass carp scales (CGCS) for effective detection of Hg(II) ions. *Microchem. J.* **2019**, *145*, 718–728. [[CrossRef](#)]
49. Tan, X.W.; Romainor, A.N.B.; Chin, S.F.; Ng, S.M. Carbon dots production via pyrolysis of sago waste as potential probe for metal ions sensing. *J. Anal. Appl. Pyrolysis* **2014**, *105*, 157–165. [[CrossRef](#)]
50. Ma, X.; Dong, Y.; Sun, H.; Chen, N. Highly fluorescent carbon dots from peanut shells as potential probes for copper ion: The optimization and analysis of the synthetic process. *Mater. Today Chem.* **2017**, *5*, 1–10. [[CrossRef](#)]
51. Zhou, J.; Sheng, Z.; Han, H.; Zou, M.; Li, C. Facile synthesis of fluorescent carbon dots using watermelon peel as a carbon source. *Mater. Lett.* **2012**, *66*, 222–224. [[CrossRef](#)]
52. Varsha Raveendran, P.T.; Renuka, N.K. Hydrothermal synthesis of biomass-derived carbon nanodots: Characterization and applications. *Mater. Chem. Phys.* **2022**, *288*, 126236. [[CrossRef](#)]
53. Krishnaiah, P.; Atchudan, R.; Perumal, S.; Salama, E.-S.; Lee, Y.R.; Jeon, B.-H. Utilization of waste biomass of *Poa pratensis* for green synthesis of n-doped carbon dots and its application in detection of  $Mn^{2+}$  and  $Fe^{3+}$ . *Chemosphere* **2022**, *286*, 131764. [[CrossRef](#)]
54. Sajjan, D.; Binoy, J.; Pradeep, B.; Venkata Krishna, K.; Kartha, V.B.; Joe, I.H.; Jayakumar, V.S. NIR-FT Raman and infrared spectra and ab initio computations of glycinium oxalate. *Spectrochim. Acta Part A Mol. Biomol. Spectrosc.* **2004**, *60*, 173–180. [[CrossRef](#)]
55. Huang, K.; He, Q.; Sun, R.; Fang, L.; Song, H.; Li, L.; Li, Z.; Tian, Y.; Cui, H.; Zhang, J. Preparation and application of carbon dots derived from cherry blossom flowers. *Chem. Phys. Lett.* **2019**, *731*, 136586. [[CrossRef](#)]
56. Wei, G.; Zhao, Z.; Du, J.; Li, P.; Sun, Z.; Huo, L.; Gao, Y. Reed-derived fluorescent carbon dots as highly selective probes for detecting  $Fe^{3+}$  and excellent cell-imaging agents. *RSC Adv.* **2019**, *9*, 21715–21723. [[CrossRef](#)]
57. Gao, S.; Wang, X.; Xu, N.; Lian, H.; Xu, L.; Zhang, W.; Xu, C. From coconut petiole residues to fluorescent carbon dots via a green hydrothermal method for  $Fe^{3+}$  detection. *Cellulose* **2021**, *28*, 1647–1661. [[CrossRef](#)]
58. Kurdekar, A.; Chunduri, A.; Bulagonda, P.; Haleyrigirisetty, M.; Kamisetti, V.; Hewlett, I. Comparative performance evaluation of carbon dot-based paper immunoassay on Whatman filter paper and nitrocellulose paper in the detection of HIV infection. *Microfluid. Nanofluid.* **2016**, *20*, 99. [[CrossRef](#)]
59. Nyquist, R.A. *Infrared Spectra of Inorganic Compounds (3800–45  $cm^{-1}$ )*; Nyquist, R.A., Kagel, R.O., Eds.; Academic Press: New York, NY, USA, 1971.
60. Margoshes, M.; Fassel, V.A. The infrared spectra of aromatic compounds: I. The out-of-plane C-H bending vibrations in the region 625–900  $cm^{-1}$ . *Spectrochim. Acta* **1955**, *7*, 14–24. [[CrossRef](#)]
61. Pena, A.C.C.; Raymundo, L.M.; Trierweiler, L.F.; Gutterres, M. Green carbon dots synthesized from *Chlorella Sorokiniana* microalgae biochar for chrome detection. *J. Ind. Eng. Chem.* **2023**, *117*, 130–139. [[CrossRef](#)]
62. Elamin, N.Y.; Modwi, A.; Abd El-Fattah, W.; Rajeh, A. Synthesis and structural of  $Fe_3O_4$  magnetic nanoparticles and its effect on the structural optical, and magnetic properties of novel Poly(methyl methacrylate)/Polyaniline composite for electromagnetic and optical applications. *Opt. Mater.* **2023**, *135*, 113323. [[CrossRef](#)]
63. Nadafan, M.; Sabbaghan, M.; Ahmadi, Z. Role of donor/acceptor of doping on nonlinear optical properties of CdS nanocomposite decorated by carbon quantum dots and reduced graphene oxide. *Diam. Relat. Mater.* **2024**, *146*, 111136. [[CrossRef](#)]
64. Diwan, I.; Tripathi, G.K.; Khare, P.S. Synthesis of green fluorescent, energy efficient nitrogen doped carbon quantum dots. *Optik* **2024**, *303*, 171725. [[CrossRef](#)]
65. Ngu, P.Z.Z.; Chia, S.P.P.; Fong, J.F.Y.; Ng, S.M. Synthesis of carbon nanoparticles from waste rice husk used for the optical sensing of metal ions. *New Carbon Mater.* **2016**, *31*, 135–143. [[CrossRef](#)]
66. Bhattacharya, A.; Chatterjee, S.; Khorwal, V.; Mukherjee, T.K. Luminescence turn-on/off sensing of biological iron by carbon dots in transferrin. *Phys. Chem. Chem. Phys.* **2016**, *18*, 5148–5158. [[CrossRef](#)]
67. Fong, J.F.Y.; Chin, S.F.; Ng, S.M. A unique “turn-on” fluorescence signalling strategy for highly specific detection of ascorbic acid using carbon dots as sensing probe. *Biosens. Bioelectron.* **2016**, *85*, 844–852. [[CrossRef](#)]
68. Liu, Y.; Zhao, Y.; Zhang, Y. One-step green synthesized fluorescent carbon nanodots from bamboo leaves for copper (II) ion detection. *Sens. Actuators B Chem.* **2014**, *196*, 647–652. [[CrossRef](#)]
69. Zaman, A.S.K.; Tan, T.L.; Jamaludin, N.; Sadrolhosseini, A.R.; Rashid, U.; Rashid, S.A. Properties and molecular structure of carbon quantum dots derived from empty fruit bunch biochar using a facile microwave-assisted method for the detection of  $Cu^{2+}$  ions. *Opt. Mater.* **2021**, *112*, 110801. [[CrossRef](#)]
70. Zhao, Y.; Jing, S.; Peng, X.; Chen, Z.; Hu, Y.; Zhuo, H.; Sun, R.; Zhong, L. Synthesizing green carbon dots with exceptionally high yield from biomass hydrothermal carbon. *Cellulose* **2020**, *27*, 415–428. [[CrossRef](#)]
71. Sha, Y.; Lou, J.; Bai, S.; Wu, D.; Liu, B.; Ling, Y. Hydrothermal synthesis of nitrogen-containing carbon nanodots as the high-efficient sensor for copper (II) ions. *Mater. Res. Bull.* **2013**, *48*, 1728–1731. [[CrossRef](#)]
72. Rooj, B.; Dutta, A.; Islam, S.; Mandal, U. Green synthesized carbon quantum dots from *Polianthes tuberosa* L. Petals for Copper (II) and Iron (II) detection. *J. Fluoresc.* **2018**, *28*, 1261–1267. [[CrossRef](#)]
73. Das, P.; Ganguly, S.; Bose, M.; Mondal, S.; Das, A.K.; Banerjee, S.; Das, N.C. A simplistic approach to green future with eco-friendly luminescent carbon dots and their application to fluorescent nano-sensor ‘turn-off’ probe for selective sensing of copper ions. *Mater. Sci Eng. C Mater. Biol. Appl.* **2017**, *75*, 1456–1464. [[CrossRef](#)]
74. Patir, K.; Gogoi, S.K. Nitrogen-doped carbon dots as fluorescence ON–OFF–ON sensor for parallel detection of copper(ii) and mercury(ii) ions in solutions as well as in filter paper-based microfluidic device. *Nanoscale Adv.* **2019**, *1*, 592–601. [[CrossRef](#)]

75. Wang, Z.; Xiao, X.; Zou, T.; Yang, Y.; Xing, X.; Zhao, R.; Wang, Z.; Wang, Y. Citric Acid Capped CdS Quantum Dots for Fluorescence Detection of Copper Ions (II) in Aqueous Solution. *Nanomaterials* **2018**, *9*, 32. [[CrossRef](#)]
76. Wang, F.; Gu, Z.; Lei, W.; Wang, W.; Xia, X.; Hao, Q. Graphene quantum dots as a fluorescent sensing platform for highly efficient detection of copper(II) ions. *Sens. Actuators B Chem.* **2014**, *190*, 516–522. [[CrossRef](#)]
77. Zheng, X.; Liu, W.; Gai, Q.; Tian, Z.; Ren, S. A Carbon-Dot-Based Fluorescent Probe for the Sensitive and Selective Detection of Copper(II) Ions. *ChemistrySelect* **2019**, *4*, 2392–2397. [[CrossRef](#)]
78. Li, Y.; Chen, J.; Wang, Y.; Li, H.; Yin, J.; Li, M.; Wang, L.; Sun, H.; Chen, L. Large-scale direct pyrolysis synthesis of excitation-independent carbon dots and analysis of ferric (III) ion sensing mechanism. *Appl. Surf. Sci.* **2021**, *538*, 148151. [[CrossRef](#)]
79. Zhang, Y.; Li, G.; Lu, M.; Li, J.; Zhou, Q.; Zou, X.; Yang, W.; Yang, M.; Wang, H. Bifunctional magnetic carbon dots for the rapid fluorescent detection and the efficient adsorptive removal of copper ion. *Microchem. J.* **2024**, *206*, 111424. [[CrossRef](#)]
80. Su, J.; Wu, L.; Zhu, Y.; Xiong, Z.; Zhao, L. Nitrogen–silicon Co-doped carbon dots synthesized based on lemon peel for copper (II) detection via a dynamic quenching mechanism. *Opt. Mater.* **2024**, *155*, 115800. [[CrossRef](#)]
81. Sharma, A.; Das, J. Small molecules derived carbon dots: Synthesis and applications in sensing, catalysis, imaging, and biomedicine. *J. Nanobiotechnol.* **2019**, *17*, 92. [[CrossRef](#)]

**Disclaimer/Publisher’s Note:** The statements, opinions and data contained in all publications are solely those of the individual author(s) and contributor(s) and not of MDPI and/or the editor(s). MDPI and/or the editor(s) disclaim responsibility for any injury to people or property resulting from any ideas, methods, instructions or products referred to in the content.